A Nature Portfolio journal



https://doi.org/10.1038/s43247-025-02260-x

Photic-zone euxinia had a major role in the Devonian-Carboniferous boundary mass extinction

Check for updates

Xiangdong Wang¹, Stephen E. Grasby², Peter A. Cawood 🖲³, He Zhao 🕞⁴ ⊠, Zhong-Qiang Chen 🕞⁵, Makram Hedhli 🕞², Zhengyi Lyu¹, Guangyi Sun 🕒 & Fang Hao⁵

Marine anoxia is widely proposed as a kill mechanism for the Devonian-Carboniferous boundary mass extinction commonly linked to the end-Devonian Hangenberg Crisis (~359.3 Ma), but the exact connections between primary drivers, marine redox conditions, and biotic turnover are not well constrained. Mercury concentrations and isotopes from multiple sections in South China and western Canada show no significant signature of enhanced volcanism during the end-Devonian Hangenberg Crisis. Rather, the distinct negative shifts of $\Delta^{199} Hg$ coupled with positive shifts of $\delta^{202} Hg$ across the end-Devonian Hangenberg Crisis provide compelling evidence for development of photic zone euxinia, as supported by covariant pyrite framboid data and Ce/Ce* values of carbonate. The photic zone euxinia was likely driven by increased nutrient delivery given its coincidence with carbon isotopic perturbations and enhanced weathering immediately before the end-Devonian Hangenberg Crisis. Our data highlight the possibility that photic zone euxinia played a pivotal role in the extinction of marine biota during the end-Devonian Hangenberg Crisis by limiting the habitable space and by increased hydrogen sulfide toxicity, especially for organisms living in shallow water.

The end-Devonian Hangenberg Crisis (EDHC; 359.3 ± 0.1 Ma with a duration of 100-300 ka) is of the same scale as the so-called 'Big Five' firstorder Phanerozoic mass extinctions, and severely impacted marine invertebrates, especially ammonoids, trilobites, conodonts, stromatoporoids, and ostracodes, and is associated with a major turnover from spore groups to seed plants on land¹⁻⁴. Climate and depositional environment also underwent remarkable changes during the latest Devonian, including abrupt glacial-interglacial fluctuations^{3,5}, widespread anoxia⁶⁻⁹, enhanced continental weathering¹⁰, widespread demise of carbonate factories^{5,8,11}, and distinct perturbations in the global carbon cycle^{3,12,13}. Enhanced terrestrial inputs due to land plant evolution could be a primary trigger for climate cooling and marine anoxia during the EDHC, through drawdown of atmospheric CO2 levels and elevated primary productivity stimulated by nutrient influx10. However, other studies have argued that enhanced volcanism played a significant role in driving climate and environment changes based on mercury (Hg) enrichments during the EDHC or in upper Devonian successions¹⁴⁻¹⁸. Therefore, the ultimate cause(s) of the EDHC remain controversial.

Marine anoxia has been commonly proposed as a potent killing mechanism for the EDHC^{3,6,7,9}. Widespread marine anoxia associated with latest Devonian black shales has been documented by various organic and inorganic proxies^{8,9,19-21}. However, it has to be noted that the Hangenberg black shales (HBS) occurred in the lower part of the Middle *Siphonodella* (S.) *praesulcata* conodont zone in Germany, whereas the EDHC lasted a much longer time spanning from the base of the Middle *S. praesulcata* zone to the base of the earliest Carboniferous *S. sulcata* zone³. A recent study in western Canada shows that the onset of anoxia and black shale deposition in western Laurentia happened much earlier (ca. 4 Ma) than other regions, and suggests the occurrence of multiple diachronous anoxic basins in the latest Devonian where biota was under stress²². Therefore, the explicit response of marine life to anoxia during the EDHC remains elusive and open for further evaluation.

¹State Key Laboratory of Geological Processes and Mineral Resources, China University of Geosciences (Wuhan), Wuhan, China. ²Geological Survey of Canada–Calgary, Natural Resources Canada, Calgary, Alberta, Canada. ³Department of Earth Atmosphere and Environment, Monash University, Melbourne, Victoria, Australia. ⁴College of Marine Science and Technology, China University of Geosciences (Wuhan), Wuhan, China. ⁵State Key Laboratory of Geomicrobiology and Environmental Changes, China University of Geosciences (Wuhan), Wuhan, China. ⁵State Key Laboratory of Environmental Geochemistry, Chinese Academy of Sciences, Guiyang, China. ⁵National Key Laboratory of Deep Oil and Gas, China University of Petroleum (East China), Qingdao, China. ⊠e-mail: hzhaocug@163.com; sunquangyi@mail.gyig.ac.cn

Mercury (Hg) has been widely used as a proxy for large-scale volcanic events as they can result in widespread Hg enrichments in sediments However, other factors, such as soil erosion and sequestration of seawater Hg under anoxic/euxinic conditions, can also cause Hg anomalies in sedimentary rocks^{23–26}. Thus, clarifying the sources of Hg in seawater and/or sediments is crucial to our understanding of the causal relationships between extinction events and coeval geological processes. Hg isotopes are a powerful tool to trace Hg sources and pathways in sediments as it exhibits both mass-dependent (MDF) and mass-independent fractionations (MIF)²⁷. To date, Hg isotopes have been successfully applied to trace past-volcanic events^{25,28,29}, enhanced soil erosion^{25,26}, and development of photiczone euxinia^{30–34} throughout the Earth history. Hg isotopes from an Upper Devonian and Lower Carboniferous drillcore section in Tennessee (USA) show multiple negative excursions in MIF (Δ^{199} Hg) along with concurrent positive shifts in MDF (δ^{202} Hg), providing evidence for photic-zone euxinia

events in the late Devonian and early Carboniferous oceans³¹. However, the EDHC beds in the studied core are either missing or have not been identified by biostratigraphy³¹, making it difficult to link seawater redox conditions with the EDHC. Hence, detailed Hg isotopes across the EDHC are required to unravel if there is a volcanic signature across the EDHC and to investigate how variations in seawater redox conditions related to the EDHC.

Here, we selected two Devonian-Carboniferous boundary (DCB) sections in South China, namely the Longan section that lies on the Qianggui carbonate platform and the Duli section that is situated in the Youjiang basin (Fig. 1), and one section at Jura Creek in Western Canada that lies within an interpreted inner-ramp setting²². These varied depositional settings from different tectonic domains enable a globally spatial view of the EDHC. We used carbon isotopes to monitor carbon-cycle disturbances and for stratigraphic correlation, and Hg isotopes to determine the sources and depositional pathways of seawater Hg and its response to the

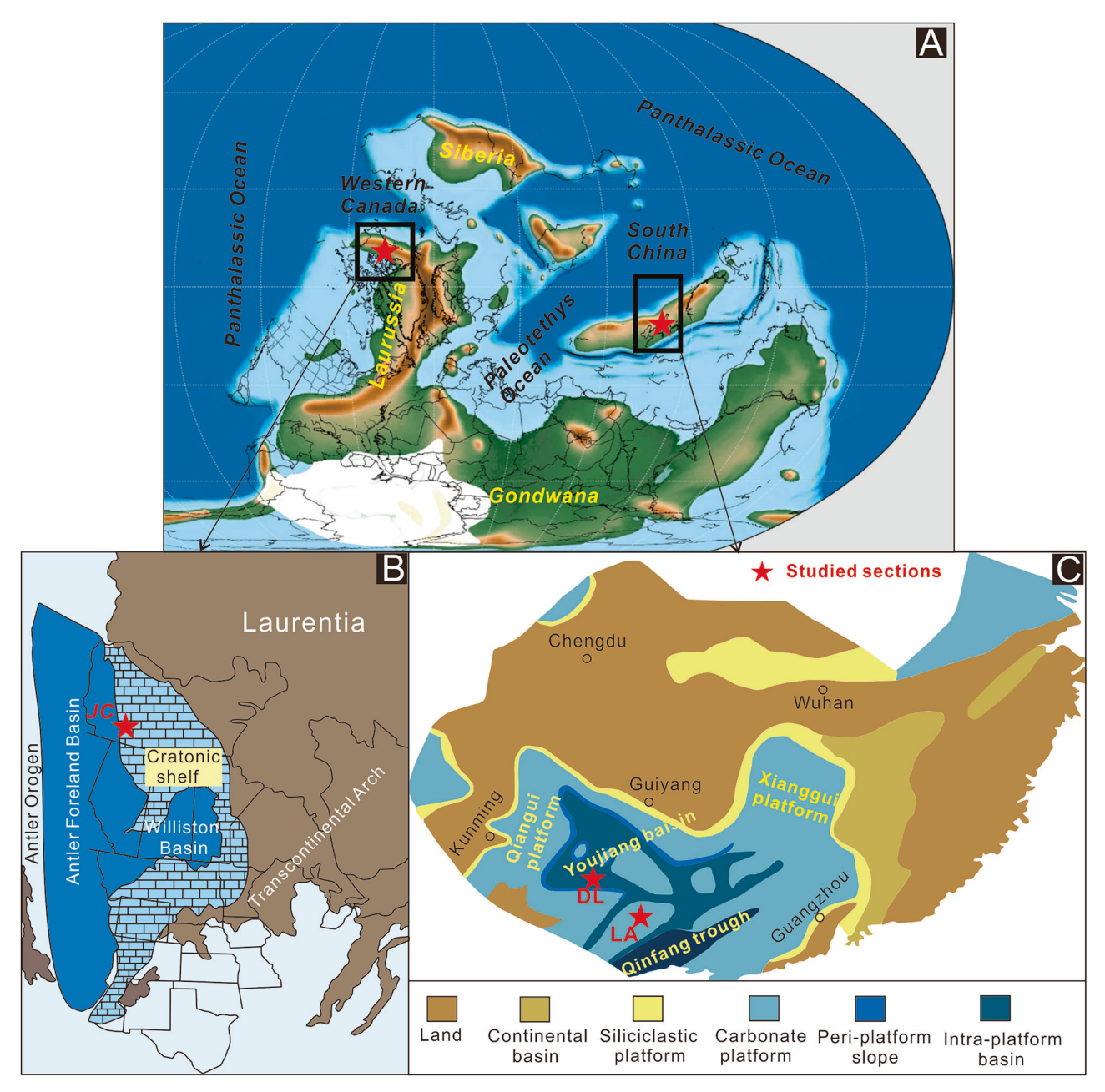


Fig. 1 | Latest Devonian paleogeographic reconstructions. A global paleogeographic reconstruction showing the location of South China and Western Canada (base map from https://deeptimemaps.com authorized by Colorado Plateau

Geosystems Inc.); **B** Paleogeographic reconstruction of Western Laurentia showing location of the Jura Creek (JC) section⁶¹; **C** Paleogeographic map of South China craton showing localities of Longan (LA) and Duli (DL) sections¹².

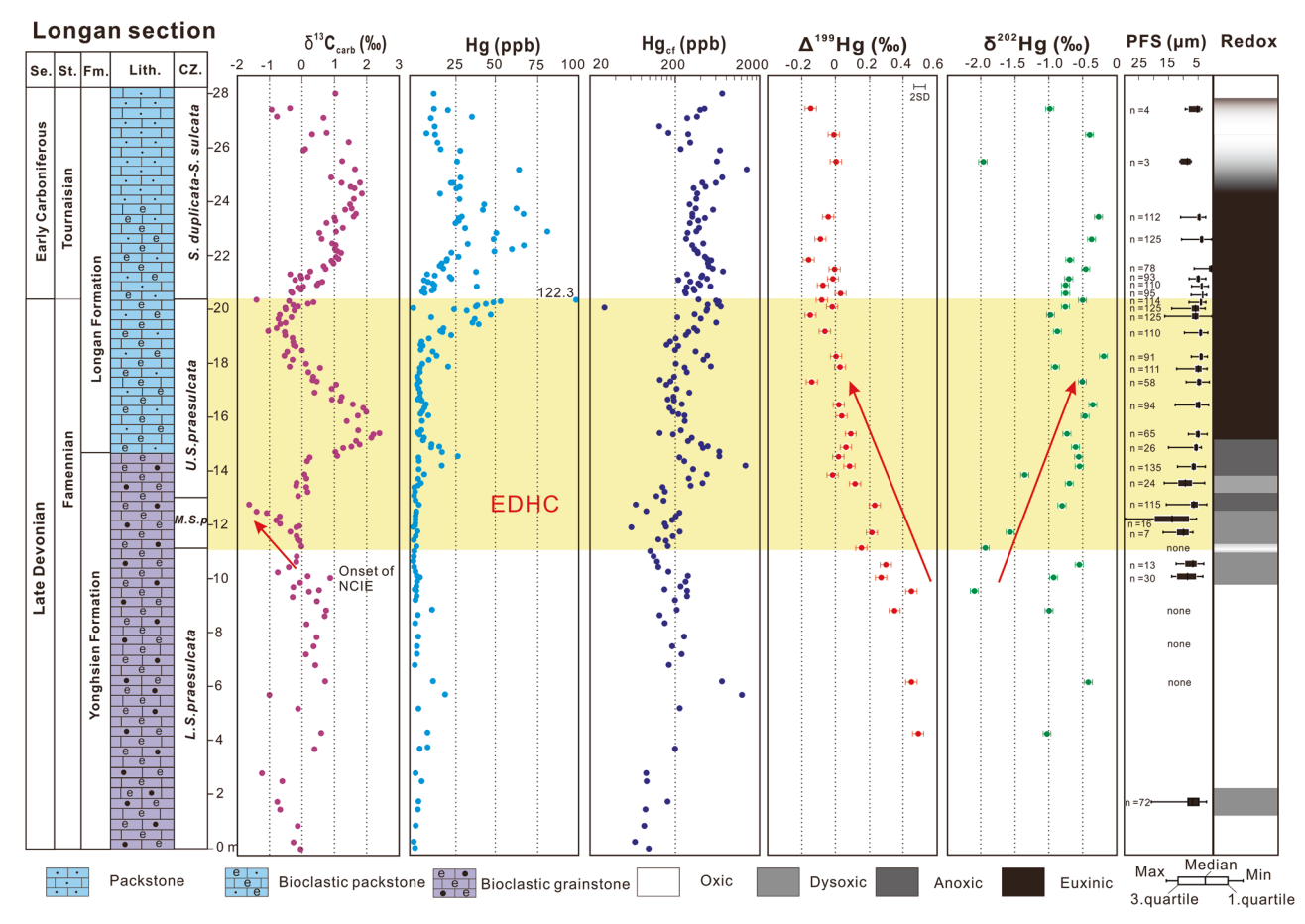


Fig. 2 | Stratigraphic information and geochemical profiles in Longan from South China. Including lithology, conodont zones 12 , inorganic carbon isotope $(\delta^{13}C_{carb})$, whole rock Hg concentration, carbonate-free Hg concentration (Hg_{cf}), $\Delta^{199}\text{Hg}$, $\delta^{202}\text{Hg}$ and pyrite framboids size (PFS) data. Se. Series, St. Stages, Fm.

Formation, Lith. Lithology, CZ Conodont zones, L. S. praesulcate Lower Siphonodella praesulcate, M. S. p Middle Siphonodella praesulcate, U. S. p Upper Siphonodella praesulcate, EDHC End-Devonian Hangenberg Crisis, NCIE Negative carbon isotopic excursion, SD standard deviation.

marine anoxia. We also measured major and trace elements to provide insights into changes of compositions in the studied samples and applied Ce/Ce* as well as size distribution of pyrite framboids to trace the redox state of the water column in studied sites^{35–38}, and used chemical index of alteration (CIA) data in Jura Creek to evaluate weathering intensity changes across the DCB³⁹. This data set provides a window to observe the Hg cycle across the DCB and the causes and consequences of the EDHC.

Results

In the Longan section, values of $\delta^{13}C_{carb}$ are ~ 0 ‰ in the Lower S. praesulcate conodont zone, whereas they shift to negative values from the uppermost segment of the Lower S. praesulcate zone to the minimum of -1.63% during the Middle S. praesulcate zone, followed by a positive excursion to the maximum of 2.39% during the Upper S. praesulcate zone (Fig. 2). The $\delta^{13}C_{carb}$ values return to ~0% at the end of Upper S. praesulcate zone and show the second positive excursion during the Tournaisian (S. duplicate-S. sulcata zone; Fig. 2). Hg concentrations in this section vary from 1.3 ppb to 122.3 ppb with low values (less than 25 ppb) in Lower to Middle S. praesulcate conodont zones, but with elevated values at the end of Upper S. praesulcate zone, and higher values (up to 80.9 ppb) in the Tournaisian (Fig. 2). Both Δ^{199} Hg and δ^{202} Hg show large variations in Longan, with Δ^{199} Hg ranging from $-0.16 \pm 0.06\%$ to $0.49 \pm 0.06\%$ and δ^{202} Hg ranging from $-2.10 \pm 0.07\%$ to $-0.19 \pm 0.07\%$ (Fig. 2). The background values of Δ^{199} Hg in the Lower S. praesulcate zone are ~ 0.4 % and show a shift from the uppermost Lower S. praesulcate zone to lower values ($\sim 0.2\%$) at the base of the Middle S. praesulcate zone (Fig. 2). δ^{202} Hg is more varied in the Lower S. praesulcate zone with values ranging from

-2.10% to -0.42%. During the Middle to Upper *S. praesulcate* zones, which correspond to the EDHC interval, Δ^{199} Hg values show a continuous decline from $\sim 0.20\%$ to $\sim -0.15\%$ and δ^{202} Hg values show a $\sim 1.8\%$ positive shift from $\sim -2.0\%$ to $\sim -0.2\%$ (Fig. 2). Values of Δ^{199} Hg remain negative ($\sim -0.2\%$ to 0%) and values of δ^{202} Hg retain high values (> -1%) except for one value of $-1.98 \pm 0.07\%$ in the Tournaisian (*S. duplicata-S. sulcata*; Fig. 2). The samples in the lower and middle part of the Lower *S. praesulcate* zone are largely devoid of pyrite framboids. However, framboid abundance increases and framboid size declines from the uppermost Lower *S. praesulcate* zone to the lower part of *S. duplicata-S. sulcata* zones (Fig. 2).

In the Duli section, values of $\delta^{13}C_{carb}$ are relatively constant at ~2% below Bed 7 (Lower S. praesulcate zone), but commence a negative shift at Bed 7 and reach the most negative value (-3.4%) in Bed 9 (costatus-kockeli interregnum; Fig. 3). The values return to -2% to 0% in beds 11-15 of the Tournaisian (S. sulcata-S. crenulata zones; Fig. 3). Hg concentrations in this section vary from 40.7 ppb to 4330.3 ppb with relatively low values (mostly less than 200 ppb) in the limestones of both the Wuzhishan and Wangyou formations, whereas peaks (more than 2000 ppb) occur in calcareous mudstones and black shales at the top of the Wuzishan Formation (Fig. 3). Values of Δ^{199} Hg vary from $-0.19 \pm 0.08\%$ to $0.18 \pm 0.08\%$ through the Duli section, and show the onset of a negative shift at the bottom of Bed 8, corresponding to the onset of negative carbon isotopic excursion (NCIE; Fig. 3). The values shift to $\sim -0.1\%$ in calcareous mudstones and black shales at the top of the Wuzishan Formation and reach the most negative values in the earliest Tournaisian (Fig. 3). Values of δ^{202} Hg display synchronous variations with those of Δ^{199} Hg, with negative values $(-1.42 \pm 0.10\%)$ to $-0.36 \pm 0.10\%$) in beds 1-7, and show the onset of a

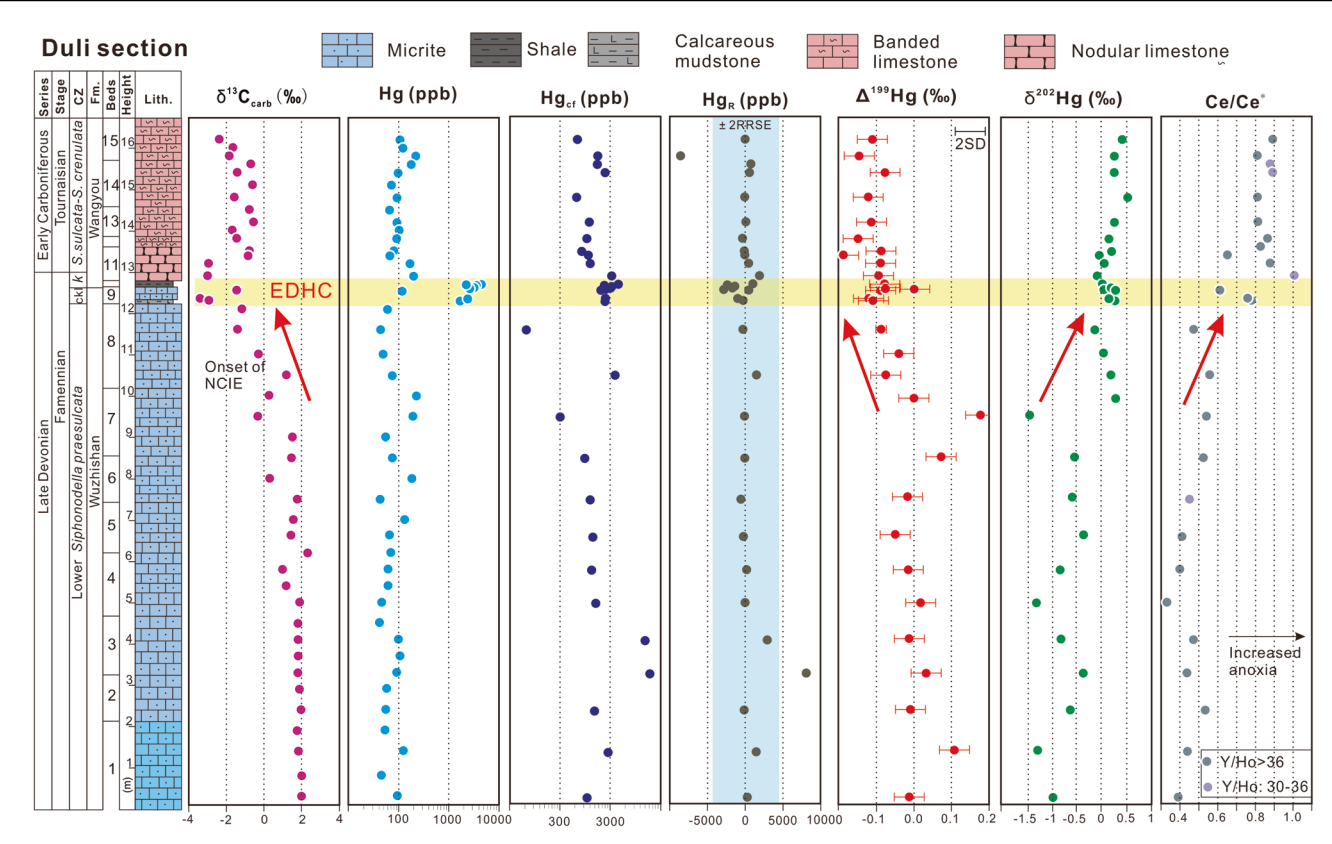


Fig. 3 | Stratigraphic information and geochemical profiles in Duli from South China. Including lithology, conodont zones 16,62 , inorganic carbon isotope $(\delta^{13}C_{carb})$, whole rock Hg concentration, carbonate-free Hg (Hg_{cf}) concentration, residual Hg (Hg_R), Δ^{199} Hg, δ^{202} Hg and Ce/Ce* values. CZ Conodont zones, $\mathit{ck}I$

costatus-kockeli interregnum, k kockli, S. Siphonodella, EDHC End-Devonian Hangenberg Crisis, NCIE Negative carbon isotopic excursion, RRSE robust residual standard error, SD standard deviation.

positive shift at the commencement of the NCIE (Fig. 3). They achieve positive values (up to $0.28\pm0.10\%$) in calcareous mudstones and black shales at the top of the Wuzishan Formation and show the most positive values (up to $0.52\pm0.10\%$) in the Wangyou Formation of the earliest Tournaisian (Fig. 3). The Ce/Ce* profile show a similar trend to that of $\delta^{202}\text{Hg}$, displaying elevated values from the upper part of Bed 7 to the peak values in the Tournaisian (Fig. 3).

In the Jura Creek section, Hg concentrations are low (~10 ppb) in the limestones of the Palliser Formation, however show peaks (up to 1605 ppb) at the bottom of the black shales. Moving up through the section, Hg concentrations progressively declined and have low values (less than 10 ppb) in calcareous mudstones, siltstones and sandstones (Fig. 4). Values of Δ^{199} Hg and δ^{202} Hg show synchronous changes through the Jura Creek section with $a \sim 0.3\%$ negative shift from $0.19 \pm 0.06\%$ in the Palliser Formation to -0.10 ± 0.06 % at the base of the black shales of the Exshaw Formation in Δ^{199} Hg and $a \sim 1.35\%$ positive shift from $-1.18 \pm 0.07\%$ to 0.18 ± 0.07 ‰ in δ^{202} Hg (Fig. 4). Upward through the section, Δ^{199} Hg and δ^{202} Hg return to less negative values (-0.05% to 0%) and more negative values (-1% to -0.5%) in the lower part of the Exshaw Formation, respectively. Hg isotope values are then more negative (as low as $-0.12 \pm 0.06\%$) for Δ^{199} Hg and less negative values ($\sim -0.5\%$) in δ^{202} Hg near the DCB. In the Tournaisian siltstones and sandstones, values of Δ^{199} Hg and δ^{202} Hg shift to $0.01 \pm 0.01\%$ (n = 2) and $-1.99 \pm 0.08\%$ (n = 2), respectively (Fig. 4). CIA varies from 56.5 to 76.7 through the Jura Creek section with relatively higher values across the DCB (Fig. 4).

Discussions

No evidence for overwhelming volcanism as a driver of the EDHC

Recent^{10,12,14} studies together with our work show that the EDHC is characterized by a negative excursion followed by a positive shift in $\delta^{13}C_{carb}$ in the Paleo-Tethys ocean (Figs. 2, 3 and S1). The negative excursion in $\delta^{13}C_{carb}$

observed at well-preserved stratigraphic successions in South China may be the result of enhanced continental weathering that stimulated organic matter respiration 10 . This process would contribute abundant $^{12}\text{C-enriched}$ dissolved inorganic carbon to the oceans 10 . In addition, release of $^{12}\text{C-enriched}$ gases from volcanic eruptions is thought to have also contributed to the negative shift in $\delta^{13}\text{C}_{\text{carb}}$, given high Hg concentrations during the EDHC 14 . Below we assess the relative importance of the two processes on the EDHC from our and published Hg and weathering data.

Profiles of whole rock Hg concentration display inconsistent variations across the DCB. In Longan, the peaks occur at the end of the EDHC and in the early Tournaisian (the uppermost of Upper S. praesulcata zone and S. duplicata-S. sulcata zones), whereas those in Duli and Jura Creek, respectively, appear during the EDHC (costatus-kockeli interregnum and Upper S. praesulcata zone) and the basal Exshaw Formation that is at least 4 Ma earlier than the EDHC based on bentonite U-Pb ages²² (Figs. 2, 3 and 4). The EDHC in Jura Creek might be within the upper part of the Exshaw black shale, based on continuous black shale deposition (Fig. 4). The discordance in Hg enrichments in whole rock data likely are associated with lithological changes given that the shifts to higher Hg concentrations correspond to changes from carbonates to shales in both Duli and Jura Creek (Figs. 3 and 4). Analysis of Hg data on a carbonate-free basis is important because increasing CaCO3 concentration can dilute non-carbonate compounds (including Hg, total organic carbon (TOC), aluminum (Al), and total sulphur (TS))⁴⁰. These increasing concentrations can force negative correlations of non-carbonate vs carbonate compounds as well as positive correlations among non-carbonate elements⁴⁰. The clear negative correlations between CaO content and Hg concentration and positive correlations between Al content and Hg concentration in all studied sections indicate that increasing CaCO₃ concentration played an important role in measured Hg concentrations (Figs. S2 and S3). Carbonate-free values (Hgcf TOCcf)

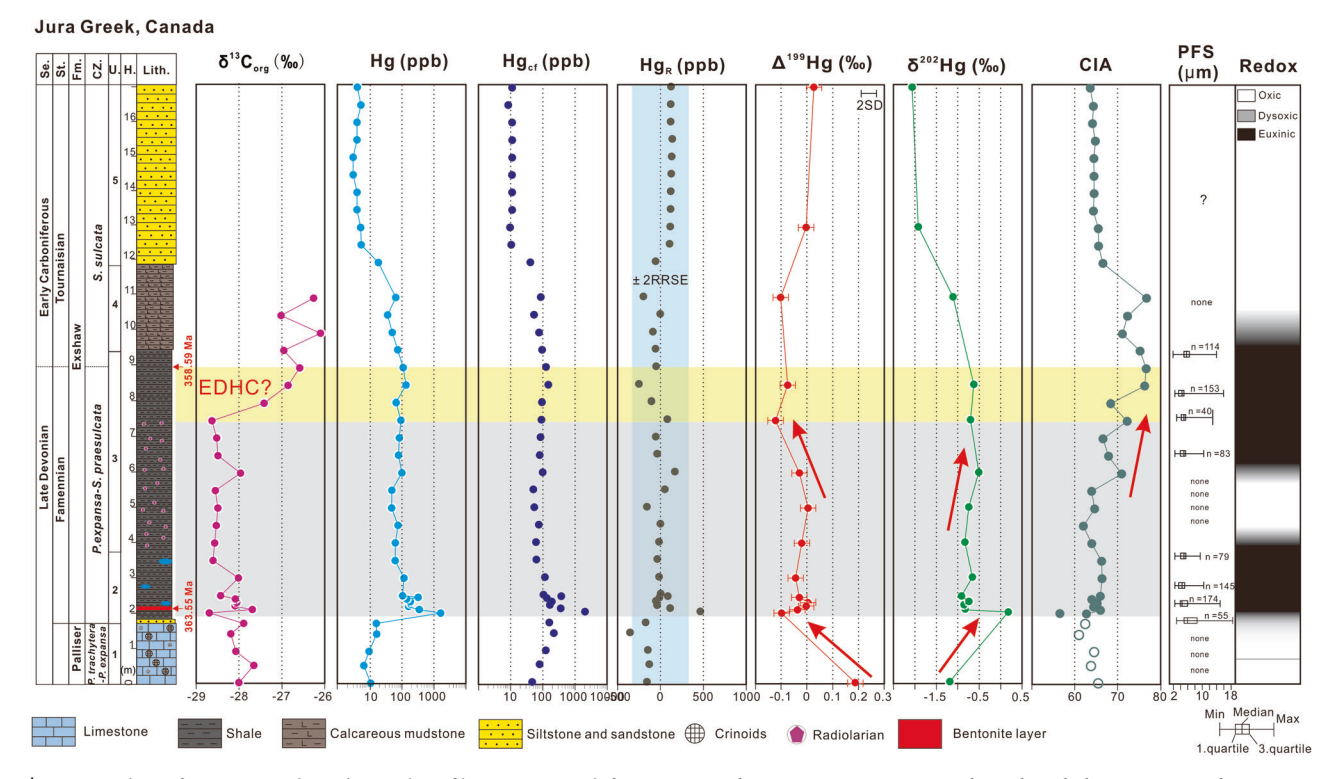


Fig. 4 | Stratigraphic information and geochemical profiles in Jura Creek from Canada. Including lithology, conodont zones 22 , $\delta^{13}C_{org}^{22}$, whole rock Hg concentration, carbonate-free Hg concentration (Hg_{cf}), residual Hg (Hg_R), Δ^{199} Hg, δ^{202} Hg and pyrite framboids data 8 . Se. Series, St. Stages, Fm. Formation, CZ

Conodont zones, U. Unit, H. Height, Lith. Lithology, EDHC End-Devonian Hangenberg Crisis, RRSE robust residual standard error, PFS pyrite framboids size, SD standard deviation.

TS_{cf} and Al_{cf}) are calculated based on measured CaO concentration (the computational formula based on previous study⁴⁰ and outlined in Supplementary Note S1). Results show that there is a rise in Hg_{cf} in the middle part of the EDHC in Longan (Fig. 2), however, the shale beds during the EDHC in Duli and the shale layers near the DCB in Jura Creek show insignificant enrichments when compared to background values of carbonate layers (Figs. 3 and 4). We also calculated residual (excess) Hg (Hg_R) in Duli and Jura Creek (follow previous method⁴⁰ and outlined in Supplementary Note S2) based on a strong linear correlation between Hgcf and TOCcf in Duli and a strong linear correlation between Hg_{cf} and TS_{cf} in Jura Creek (Fig. S4). Values of Hg_R across the DCB at both the sections are within ± 2 robust residual standard error (Figs. 3 and 4), which suggest that the Hg data is at "background" concentrations and not significantly elevated due to external processes such as volcanism⁴⁰. The synchronous changes between Hgcf and TOCcf (or TScf) as well as the lack of obvious anomalies either in Hg/TOC or Hg/TS across the EDHC in Duli and Jura Creek (Figs. S5 and S6) further indicate Hg concentrations of both the sections were highly controlled by environmental changes rather than Hg loading. In Longan, Hg_{cf} shows no correlations (R² ≤ 0.03) with TOC_{cf}, Al_{cf} and TS_{cf} (Fig. S4), making it difficult to determine the main host-phase of Hg. However, the higher Hgcf values during the Upper S. praesulcata zone and S. duplicata-S. sulcata zones correspond to distinctly elevated values in TOCcf and Al_{cf} concentrations (Fig. S7). Profile of Hg/TOC show insignificant enrichments during the EDHC (Fig. S7), though most of TOC concentrations in Longan are less than 0.2 % that would produce large uncertainty²³. In addition, the onset of negative shift in $\delta^{13}C_{carb}$ and the EDHC clearly predated higher Hgcf values of the Longan section in South China (Fig. 2), which discounts volcanism as a major driver of the EDHC even if volcanic Hg loading could have contributed to the higher Hg_{cf} values in Longan. An upper Devonian section in Illinois basin (USA) that is dominated by shales also lack Hg/TOC anomalies across the DCB (Fig. S8)31, and a well calibrated shale section (Sjol core) for the EDHC in Williston basin (USA) has elevated Hg concentrations but lacks obvious Hg/TOC anomalies (less than 30 ppb/

% and similar to background values) during the EDHC (Fig. S8)9. Furthermore, terrestrial DCB sections in East Greenland also show no Hg enrichments across the extinction interval⁴. Therefore, it is unlikely that massive subaerial volcanism, including LIP activity, was present in the latest Devonian and triggered the EDHC, though local magmatic activity could have contributed to carbon isotopic fluctuations in Europe¹⁴. Our Hg isotopic data further indicate there was no overwhelming volcanic signature during the EDHC. Volcanic derived Hg has been shown to have original Δ^{199} Hg values close to zero^{41–43}. However, oxidized Hg (II) during photoreduction in cloud droplets can result in positive Δ^{199} Hg values in the residue Hg (II) phase that is primarily received by seawater through wet or dry deposition 27,44,45. Therefore, near-zero and positive Δ^{199} Hg values with increased Hg input in sediments are considered to reflect signatures of direct deposition and atmospheric transport of enhanced volcanic Hg loading, respectively $^{25,28,29,46-48}$. Values of Δ^{199} Hg during the EDHC in Longan have a large range from 0.21% to -0.15% with a shift from positive to negative values through that time (Fig. 2). Those during the EDHC in Duli and around the DCB in Jura Creek are -0.08 ± 0.04 ‰ (sd, n = 6) and -0.10 ± 0.02 % (sd, n = 2), respectively (Figs. 3 and 4). The negative values or shifts in Δ^{199} Hg likely indicate that Hg cycle during the EDHC was dominated by environmental changes rather than recording a direct (or overwhelming) signature of volcanism.

Lithium isotope display a rapid negative shift immediately before the onset of the EDHC in South China¹⁰, suggesting a causal relationship between enhanced weathering and the EDHC. Our CIA values (the computational formula was outlined in Supplementary Note S3) of shales in Jura Creek also display elevated values approaching the DCB (Fig. 4), corresponding to the re-development of water column anoxia that is indicated by pyrite framboids data⁸. In spite of low resolution (only 5 data from *Pseudopolygnathus granulosus* to *Siphonodella sandbergi* zones), CIA values in Illinois basin (USA) show a minor increase across the DCB⁴⁹ (Fig. S8). Hence, nutrient input along with enhanced weathering could have played a significant role in marine anoxia across the EDHC.

Photic zone euxinia across the EDHC

In South China, both the Longan and Duli sections begin to display negative shifts in Δ^{199} Hg coupled with positive shifts in δ^{202} Hg in the upper part of the Lower *S. praesulcata* zone, corresponding to the onset of the NCIE (Figs. 2 and 3). Hg–MIF (Δ^{199} Hg) is mostly controlled by photochemical processes and is unlikely to be altered by post–depositional processes, whereas, the causes of Hg–MDF (δ^{202} Hg) are more varied²⁷. The lack of obvious correlation between δ^{202} Hg with Mn/Sr and Mg/Ca at both the Longan and Duli sections (Fig. S9), indicates that the study samples are unlikely to have been altered by diagenetic transformation or dolomitization. The observations of a weak negative correlation ($R^2 = 0.11$, P < 0.05, n = 34) in Longan and a strong correlation ($R^2 = 0.61$, P < 0.0005, n = 31) in Duli between Δ^{199} Hg and δ^{202} Hg (Fig. S10) further suggest the Hg isotopic compositions represent primary signals and the changes in Δ^{199} Hg and δ^{202} Hg were mainly controlled by common mechanisms.

Modern observations show atmospheric Hg (0) has higher δ^{202} Hg and lower Δ199Hg values than atmospheric Hg (II)50. Different fractions of uptake of atmospheric Hg (0) in vegetation and wet/dry deposition of atmospheric Hg (II) onto the Earth's surface results in more negative δ^{202} Hg and Δ^{199} Hg values in terrestrial than in marine reservoirs⁵⁰. Therefore, the observed negative shifts in Δ^{199} Hg and concurrent positive shifts in δ^{202} Hg cannot be explained only by increased terrestrial Hg input as that would contribute more negative δ^{202} Hg values rather than significant positive shifts (more than 1‰) as observed in the study samples (Figs. 2 and 3). Instead, the changes in Hg isotopic composition likely reflect the development of photic zone euxinia (PZE) conditions because both photoreduction of Hg (II) complexed by reduced sulfur and enhanced sequestration and oxidation of atmospheric Hg (0) in a sulfide-rich photic zone would produce negative MIF and positive MDF in Hg (II)⁵¹⁻⁵³. Such changes in Hg isotopic compositions (negative MIF and positive MDF) have been observed in deeptime oceans associated with PZE30-34.

Our pyrite framboid data in Longan and Ce/Ce* values in Duli further demonstrate that observed negative shifts in Δ^{199} Hg coupled with positive shifts in δ^{202} Hg were driven by water column redox changes. Pyrite framboid sizes have been widely utilized to diagnose redox condition of the water column, with a small size displaying a narrow distribution occurring in euxinic settings, whereas the sizes are more variable and generally larger in dysoxic environments^{35,36}. Based on size distribution of framboids, criteria have been established to distinguish different redox states of the water column (Fig. S11)35,36. Ce anomaly (Ce/Ce*) of carbonate is another proxy for rebuilding redox changes of a water column during formation of the carbonate rocks³⁷, with less negative and even positive Ce/Ce* values in the wake of increased marine anoxia (the computational formula and theory outlined in Supplementary Note S4). However, it should be noted that Ce/ Ce* can only represent seawater information when Y/Ho are more than 36, as ratios of Y/Ho can be used to distinguish between seawater and nonseawater signatures³⁸. Given that most values of Ce/Ce* in Longan are less than 36 (Supplementary Dataset 1), compared to most of those in Duli being more than 36 (with only four data within 30-36 (Fig. 2 and Supplementary Dataset 2), we propose that the variations in Ce/Ce* at Duli record the redox changes of the water column. Both the pyrite framboids in Longan and Ce/ Ce* in Duli show anoxia gradually increased from the upper part of the Lower S. praesulcata to the S. sulcata-S. crenulata zones, as indicated by reduced sizes in framboids and elevated Ce/Ce* values (Figs. 2 and 3). The covariant relationships between Hg isotopes (Δ^{199} Hg and $\delta^{2\bar{0}2}$ Hg) with mean framboid diameters as well as Ce/Ce* values, as shown by their correlations in scatter diagrams (Fig. 5), ultimately confirm the changes in Δ^{199} Hg and δ^{202} Hg were controlled by redox changes of seawater and thus reflected the PZE condition across the EDHC, further promoting Hg isotopes as a photic zone redox proxy.

The initial deposition of black shales and development of anoxic conditions in Jura Creek have been shown to start before or during the *P. expansa* conodont zone, ca. 4 Ma earlier than the EDHC²². The anoxia was suggested to be caused by a locally restricted basin driven by mountain building in the latest Devonian²², that persisted into the earliest

Carboniferous although the bottom water was likely more oxic around the DCB than earlier as evidenced by trace metal proxies (e.g., Mo, U, and Cd)^{8,22}. Our Hg isotopic data from Jura Creek also show correlation between Δ^{199} Hg and δ^{202} Hg (R² = 0.18, p < 0.05, n = 15; Fig. S10), and $a \sim 0.3\%$ negative shift of Δ^{199} Hg coupled with $a \sim 1$ ‰ positive shift of δ^{202} Hg at the bottom of the Exshaw black shales (Fig. 4), corresponding to Mo concentration peaks²², supporting a shift to euxinic condition even in the photic zone. After a slight recovery ($\sim 0.1\%$), Δ^{199} Hg values show again $a \sim 0.1\%$ negative excursion coupled with $a \sim 0.4\%$ positive excursion in δ^{202} Hg in the uppermost *S. praesulcata* zone (Fig. 4), suggesting the PZE had continued into the EDHC. This is supported by pyrite framboids data⁸ that show euxinic water column conditions during that time in Jura Creek (Fig. 4).

Apart from our Hg isotopic data, the presence of lipid biomarkers of green sulfur bacteria in the black shales from sections in central Poland and North America provides further evidence for photic-zone euxinia 20,21 . Spatiotemporal redox trends across the entire Williston Basin (USA) during the EDHC display not only expanded water column euxinia but also euxinic seawater into shallow environments 9 . Ratios of I/Ca for a carbonate platform in South China as well show expansion of the oxygen minimum zone into the ocean-surface layer at that time 6 . Although the DCB shale beds were extremely condensed and largely lack biostratigraphic constraint 31 , a drill core section in the Illinois basin (USA) shows negative shift in $\Delta^{199}{\rm Hg}$ coupled with positive shift in $\delta^{202}{\rm Hg}$ pre-the DCB (Fig. S8), suggesting a PZE condition during that time 31 . Therefore, the development of PZE was widespread and played a significant role in organism losses across the EDHC.

Implications for causal relationship between environmental change and the EDHC

The integration of our carbon and Hg isotopes with previously published latest Devonian-earliest Carboniferous weathering proxy (lithium isotope), palaeontologic data and paleotemperature records (Fig. 6), enable a holistic assessment of environmental conditions across the EDHC. Values of lithium isotope (δ⁷Li_{carb}) as well as $\delta^{13}C_{carb}$ are relatively constant in lower-middle part of the Lower S. praesulcata zone (Fig. 6), however, both the isotopes show sudden negative shifts in the uppermost part of the Lower S. praesulcata zone (Fig. 6), ca. 90 ka before the EDHC¹⁰, indicative of enhanced silicate weathering and carbon perturbations immediately before the EDHC. Enhanced weathering is expected to increase nutrient inputs to the ocean that would contribute to oceanic eutrophication and anoxia⁵⁴. Our Hg isotopic data support PZE conditions starting to spread at the onset of the NCIE and thus was likely a consequence of enhanced weathering (Fig. 6). A PZE event is deadly to organisms living in surface waters, such as stromatoporoid and rugose coral (Fig. 7), both of which show a decline in diversity before the EDHC (Fig. 6)⁵⁵. There are small-scale but distinctive extinction episodes of conodonts and ammonoids in the immediate pre-crisis beds in Sardinia (Italy) and Rhenish Massif³, suggesting environment deterioration immediately preceding the EDHC.

A continuous and more rapid weathering was present during the Middle *S. praesulcata* zone (or *costatus-kockeli* interregnum)¹⁰, corresponding to the shifts to lower values in $\delta^{13}C_{carb}$ (Fig. 6), likely indicating enhanced ^{12}C -enriched dissolved inorganic carbon inputs along with increased weathering. Meanwhile, efficient CO₂ drawdown due to strong weathering of rocks would regulate the climate into a cooling stage as shown by $\delta^{18}O_{apatite}$ values from conodonts (Fig. 6)⁵⁶. Oberved negative shift in $\delta^{13}C_{carb}$ during the Middle *S. praesulcata* zone supports the hypothesis that the peak or onset of Hangenberg positive carbon isotopic excursion post-dated the HBS because the HPICE records burial of abundant organic matter in the deep ocean rather than in epeiric seas 57,58 . Following the decline in $\delta^{13}C_{carb}$ values, positive shifts of $\delta^{13}C_{carb}$ have been recorded within the Upper *S. praesulcata* zone, consistent with cessation of increased weathering (though the weathering was still stronger than pre-the EDHC) (Fig. 6),

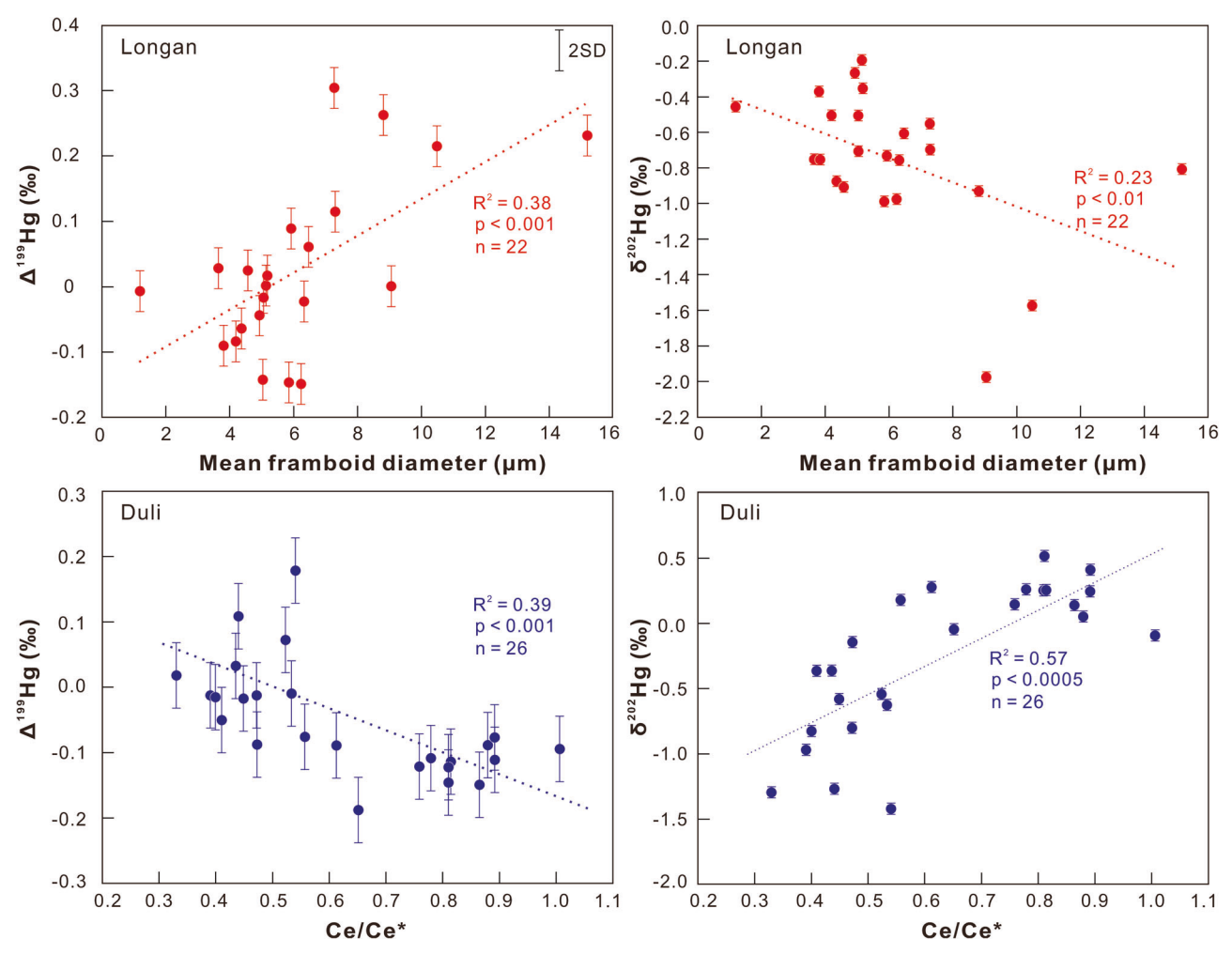


Fig. 5 | Scatter plots of Δ¹⁹⁹Hg and δ²⁰²Hg with redox proxies in Longan and Duli. Values of Δ¹⁹⁹Hg and δ²⁰²Hg show correlation with mean framboid diameter in Longan and Ce/Ce* values in Duli. SD standard deviation.

supporting the inference of large-scale sequestration of organic carbon within the Upper *S. praesulcata* zone¹². Our Hg isotopic data in South China show progressively negative shifts of Δ^{199} Hg coupled with positive shifts of δ^{202} Hg from the uppermost of the Lower *S. praesulcata* zone to the Tournaisian (Fig. 6), indicative of an enhanced PZE process through the EDHC, which is further confirmed by data from elevated Ce/Ce* values and pyrite framboids during that time (Figs. 2 and 3).

In these circumstances, the PZE was likely driven by nutrient influx and elevated primary productivity, and played an important role in the collapse of marine invertebrates during the EDHC (Fig. 7), as shown by the final demise of stromatoporoids and a large decline of biodiversity in rugose corals (Fig. 6). The development of PZE condition near the DCB triggered by increased weathering input is also indicated by the coincidence between nutrient input and Hg isotopic shifts in Illinois basin (USA)31 and by Our CIA and Hg isotope data in Jura Creek (Fig. 4). The ultimate cause of enhanced silicate weathering across the EDHC is still unknown. The absence of a global fingerprint for volcanic Hg and any record of a large igneous province during that time suggests the driving force is not linked to large-scale volcanism. In contrast, the tectonically driven basin restriction model²² and/ or the arguably rapid spread of seed plants^{59,60}, likely were a more possible trigger for the increase in weathering intensity. Emerging studies disagree with the idea that plant expansion caused anoxia, and even argue that instead it led to oxidation of the oceans⁶⁰. In any case, our Hg isotopic data from successions show a global PZE condition across the EDHC that could be an important killing mechanism for the DCB mass extinction.

Methods

Studied sections

During the Late Devonian to Early Carboniferous, paleogeographic reconstructions indicate the South China craton occupied a paleo-latitude of 0–15° S and the northwest coast of Laurentia occupied a near equatorial location of 10–15°N (Fig. 1). At that time, the southern (paleo-eastern) margin of South China developed a complex facies architecture spanning from siliciclastic platform, to carbonate platform to deep water basin (Fig. 1), whereas in western Canada, a shallow epicontinental sea covered the broad cratonic platform⁶¹.

The Longan section (23°10′34.8″N, 107°27′48.0″E) is located in Dujie Village of Long'an County in Guangxi Province, of which the lithologic, carbon isotopic and bio-stratigraphy has been well studied¹¹. The DCB succession in this section contains the Yonghsien Formation that consists mainly of massive bioclastic grainstone, and the overlying Longan Formation that is composed of thin-medium bioclastic packstone and packstone (Fig. 2). The DCB defined by the first appearance of the conodont *S. sulcata*, is located ~6 m above the base of the Longan Formation¹². Based on fossil assemblage and carbon isotopic stratigraphy, the base of the Upper *S. praesulcata* and Middle *S. praesulcata* zones are placed at ~2 m and ~3.3 m below the base of the Longan Formation, respectively^{7,12}. The Longan section was situated on a platform separated from the Yangtze paleo-landmass by the Youjiang Basin.

The Duli section (25°23′ 50.1″ N, 107°20′ 05.5″ E) is well-exposed along the X921 road, near the Duli village of Nandan County, Guangxi Province. The lithology and biostratigraphy have been described in detail⁵⁶.

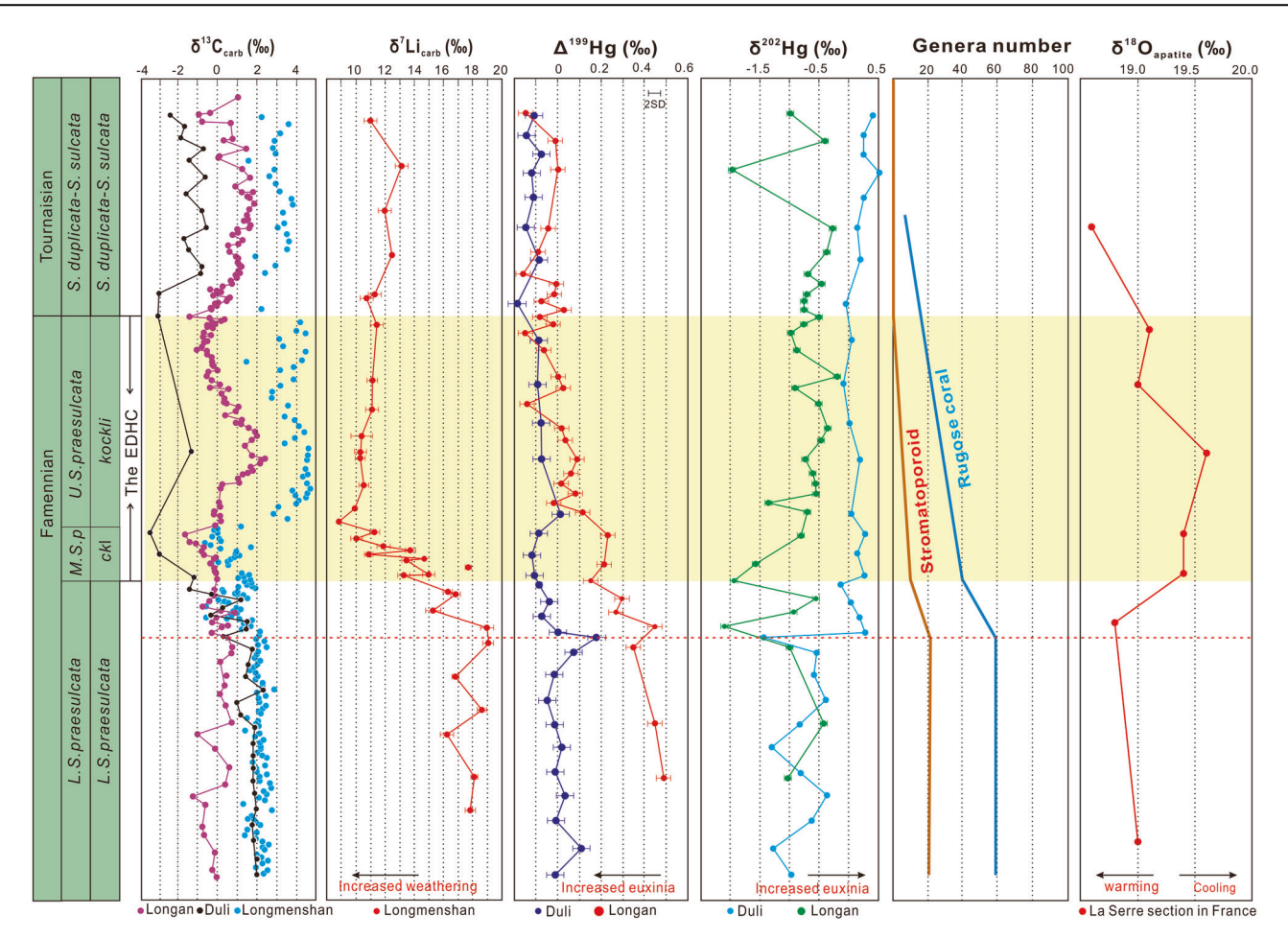


Fig. 6 | Generalized chemostratigraphic trends of the latest Devonian and the relationship to biotic change. Integrated excursions of inorganic carbon isotope $(\delta^{13}C_{carb}; Longan and Duli (this study); Longmenshan¹⁰), lithium isotope¹⁰, Hg$

isotopes (Δ^{199} Hg and δ^{202} Hg), genera number of stromatoporoid and rugose coral stromatoporoid and rugose coral strong and δ^{18} O apatite strong across the end-Devonian Hangenberg crisis. *ckI costatus-kockeli* interregnum, *k kockli*, SD standard deviation.

At this locality, the DCB succession is divided into the Wuzhishan Formation and the overlying Wangyou Formation. The Wuzhishan Formation is mainly composed of massive micrite, with rare calcareous mudstone and $a\sim 15$ cm-thick black shale at the top separating the overlying Wangyou nodular and banded limestone (Fig. 3). Conodont biostratigraphy show the Wuzhishan Formation in this section contains abundant pelagic conodonts of the Lower *S. praesulcata* Zone, whereas the Wangyou Formation spans from the Upper *S. praesulcata* Zone to the Lower *S. Crenulate* Zone with the DCB placed at ~20 cm above the top of the black shale based on the first occurrence of typical *S. sulcata* ⁶². The fine grained, condensed limestones observed in this section indicate deposition in quiet water below storm wave base, in a basinal setting ⁶².

The Jura Creek section (51°05′26″N, 115°09′29″W) is well-exposed along a tributary to the Bow River, western Alberta, Canada. The DCB succession in this stratigraphic section is composed of the Palliser Formation carbonates and the overlying Exshaw Formation that mainly consists in ascending order of black shales, calcareous mudstones, and siltstones and sandstones (Fig. 4). The conodont fauna indicates the uppermost Palliser Formation is within the *Palmatolepis* (*P.) trachytera*-lower *P. expansa* zone, and the deposition of black shales ranges from lower *P. expanse* zone to *S. praesulcata* zone (Fig. 4)^{22,51,63}. The DCB was placed at the top of black shales, corresponding to the base of the *S. sulcata* zone⁶³ (Fig. 4).

A total of 267 samples (178 for Longan, 49 for Duli and 40 for Jura Creek) were analyzed geochemically. Samples were collected from outcrop with weathered surfaces first removed. In the laboratory any remaining weathered surfaces were removed and then samples were powdered to ~200 mesh in a freeze grinding apparatus for later geochemical analysis. All

analytical data of Longan, Duli and Jura Creek sections are reported in Supplementary Datasets S1, S2 and S3, respectively.

Major and trace element analyses

Whole rock major element abundances of the Longan and Duli sections were determined by wave length dispersive X-ray fluorescence analysis of pressed powder pellets using a Panalytical Zetium XRF spectrometer at the State Key Laboratory of Geological Processes and Mineral Resources (SKLGPMR), China University of Geosciences (CUG), Wuhan. Before analysis, a muffle furnace was used to determine the loss on ignition. Experimental error was less than 5%, as monitored by measuring national reference sample GBW07132. Trace elements of the Longan and Duli sections were analyzed at SKLGPMR via ICP-MS (Agilent 7500a). The dissolution procedure follows previous method⁶⁴. The sample powder was weighed into Teflon bombs followed by adding 1 mL HNO3 and HF. Then the sealed bombs were heated at 190 °C in oven for 48 h. The solution was steamed on a 115 °C electric heating plate, followed by adding 1 mL HNO3 and evaporating to the second round of dryness. The resultant salt was redissolved by adding ~3 mL of 30% HNO3 and resealed and heated in the bomb at 190 °C for 12-24 h. The final solution was diluted to 100 g with mixture of 2% HNO3 for ICP-MS analysis. Blanks and national standards AGV-2, BHVO-2, BCR-2, RGM-2 were selected for calibrating elemental concentrations with an analytical uncertainty of better than 2% for all elements of interest. Whole rock elemental data of the Jura Creek section were measured on powdered material digested in a 2:2:1:1 acid solution of H₂O-HF-HClO₄-HNO₃ and analyzed using a PerkinElmer mass spectrometer with $\pm 2\%$ analytical error²².

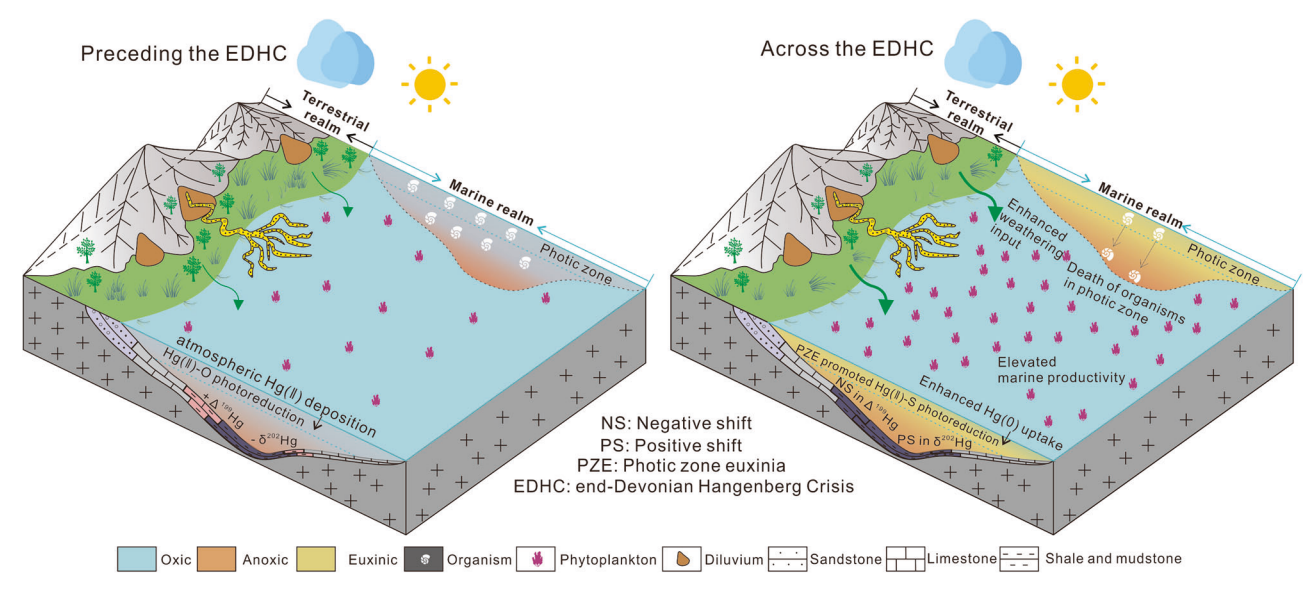


Fig. 7 | Scenario of environmental and biological changes along with Hg cycle across the end-Devonian Hangenberg Crisis (ca. 359.3 Ma).

Inorganic carbon isotopes analysis

Inorganic carbon isotopes of the Longan and Duli sections were analyzed at SKLGPMR using a MAT 253plus mass spectrometer. In preparation for carbonate carbon isotope ($\delta^{13}C_{carb}$) analysis, 80 to 120 µg of powder were placed in a 10 mL Na-glass vial, sealed with a butyl rubber septum, and reacted with 100% phosphoric acid at 72 °C after flushing with helium. The Evolved CO₂ gas was analyzed for $\delta^{13}C$. Isotope values are reported as per mile variation (‰) relative to Vienna Pee Dee belemnite standard. The analytical precision was better than 0.04‰ for $\delta^{13}C$ based on duplicate analyses of the national reference standard GBW-04416 ($\delta^{13}C = +1.61$ ‰), TB-2 ($\delta^{13}C = -6.06$ ‰).

Total organic carbon (TOC) and total sulphur (TS) analysis

TOC contents of the Longan and Duli sections were analyzed by an Elementar micro cube analyzer at the SKLGPMR in CUG. Before analysis, sample powder was digested in 2 N HCl at 50 °C for 12 h to dissolve any carbonate minerals. After multiple centrifugal and lyophilization steps, the residue was prepared for later TOC measurement. Data quality was monitored via multiple analyses of standard samples DP–1 (65.44%) and GSS-8 (1.92%), yielding an analytical precision of \pm 5 % of reported values. Values of TOC at the Jura Creek section have been published²¹. Total sulfur (TS) contents of the Longan and Duli sections were measured on a CS-902T carbon–sulfur analyzer at the State Key Laboratory of Geomicrobiology and Environmental Changes in CUG. Analytical error was within 5% based on replicate analyses of Alpha Resources standard SJSM (TS = 1.02%).

Pyrite framboid morphology analysis

We studied pyrite framboids from 31 sedimentary rock samples at the Longan section to reconstruct oceanic redox variation history through the EDHC. A polished surface (\sim 1 × 1 cm) of each sample was examined for pyrite number and sizes using a scanning electron microscope (SEM; Hitachi SU8000; its morphology under SEM please see Fig. S12) at the State Key Laboratory of Geomicrobiology and Environmental Changes in CUG. A minimum number of 100 pyrite framboid sizes was measured for each sample if possible.

Hg concentration analysis

Hg concentration analyses at Longan and Duli were conducted by a Direct Mercury Analyzer (DMA80) at the SKLGPMR in CUG. About 100 mg sample powder for limestone and ~50 mg for shales was weighed for analyses in this study. Data reliability was assessed through measurement of a standard coal sample (502–685; 40 ppb) and a repeat after 10 unknowns,

yielding an analytical precision of \pm 5% of reported Hg concentrations. Hg concentrations at Jura Creek were measured by a LECO AMA254 mercury analyzer with an analytical uncertainty of better than 10%.

Hg isotopes analysis

Hg isotopic experiments of the samples in Longan and Jura Creek were conducted by a Nu-Plasma multi-collector ICP-MS at the Institute of Geochemistry, Chinese Academy of Sciences, Guiyang, China, whereas those in Duli were analyzed using a Nu-Plasma multi-collector ICP-MS at the School of Earth System Science, Tianjin University, following the previous methods^{31,65}. The pyrolysis method was used to extract Hg from samples before Hg isotopic measurement. Sample powder was heated at 950 °C for ~3 h in a thermal decomposition furnace with oxygen injected for blowing the decomposed gaseous Hg⁰ into an absorption bottle, in which 5 mL of 40% reverse aqua regia (HCl: HNO3 = 1:3, v-v) was loaded in order to oxidize Hg (0) to Hg (II) and preserve Hg (II) with Hg recoveries of 90-110%. Concentrations between the diluted samples and bracketing standards (NIST SRM 3133) were matched within 10% that was monitored by MC-ICP-MS using 202Hg signals. NIST SRM 997 Tl was the internal standard used for simultaneous instrumental mass bias correction of Hg. The signal for ^{202}Hg was ${\sim}1.2\,\mathrm{V}$ for $1\,\text{ng/mL}$ digested solutions. Mass-dependent fractionations (MDF) of Hg isotopes are reported in δ^{202} Hg notation referenced to the NIST-3133 Hg standard⁶⁶:

$$\delta^{200} \text{Hg}(\%) = \left[\binom{202}{} \text{Hg} / \binom{198}{} \text{Hg}_{\text{sample}} \right) / \binom{202}{} \text{Hg} / \binom{198}{} \text{Hg}_{\text{standard}} \right) - 1 \right] \times 1000 \tag{1}$$

mass–independent fractionations (MIF) of Hg isotopes are expressed in Δ notation (Δ^{xxx} Hg), which describes the difference between the measured δ^{xxx} Hg and the theoretically predicted δ^{xxx} Hg value, using the following equations:

$$\Delta^{199}$$
Hg $\approx \delta^{199}$ Hg $- (\delta^{202}$ Hg $\times 0.2520)$ (2)

$$\Delta^{200} Hg \approx \delta^{200} Hg - (\delta^{202} Hg \times 0.5024)$$
 (3)

$$\Delta^{201} Hg \approx \delta^{201} Hg - (\delta^{202} Hg \times 0.7520)$$
 (4)

To ensure data quality, standard reference SRM GSS-5 prepared during the pyrolysis dissolution produced results (n=2) of δ^{202} Hg = $-1.33 \pm 0.04\%$ (2 sd); Δ^{199} Hg = $-0.29 \pm 0.03\%$ (2 sd);

 $\Delta^{200} {\rm Hg} = 0.01 \pm 0.02\%$ (2 sd); $\Delta^{201} {\rm Hg} = -0.31 \pm 0.02\%$ (2 sd) that are comparable with previous results 65 . Replicate analysis of the NIST 3177 Hg intra lab isotope reference standard produced results (n=16) of $\delta^{202} {\rm Hg} = -0.50 \pm 0.07$ % (2 sd); $\Delta^{199} {\rm Hg} = -0.01 \pm 0.06$ % (2 sd); $\Delta^{200} {\rm Hg} = 0.00 \pm 0.05\%$ (2 sd); $\Delta^{201} {\rm Hg} = -0.03 \pm 0.04\%$ (2 sd) that agree well with previous results $^{67-69}$. The averages for all analyses of NIST 8610 were (n=11): $\delta^{202} {\rm Hg} = -0.55 \pm 0.08\%$ (2 sd); $\Delta^{199} {\rm Hg} = -0.02 \pm 0.05\%$ (2 sd); $\Delta^{200} {\rm Hg} = 0.01 \pm 0.03\%$ (2 sd); $\Delta^{201} {\rm Hg} = -0.04 \pm 0.04$ % (2 sd), consistent with published values 31 .

Data availability

The authors declare that all data reported this study are available at https://doi.org/10.6084/m9.figshare.28588841 or Supplementary Datas 1, 2 and 3.

Received: 2 October 2024; Accepted: 28 March 2025; Published online: 12 April 2025

References

- Myrow, P. M. et al. High-precision U-Pb age and duration of the latest Devonian (Famennian) Hangenberg event, and its implications. *Terra Nova* 26, 222-229 (2014).
- McGhee, G. R. Jr et al. A new ecological-severity ranking of major Phanerozoic biodiversity crises. *Palaeogeogr. Palaeoclimatol. Palaeoecol.* 370, 260–270 (2013).
- Kaiser, S. I., Aretz, M. & Becker, R. T. The global Hangenberg Crisis (Devonian–Carboniferous transition): review of a first-order mass extinction. Geo. Soc. London, Special Pub. 423, 387–437 (2016).
- Marshall, J. E. A. et al. UV-B radiation was the Devonian-Carboniferous boundary terrestrial extinction kill mechanism. Sci. Adv. 6, eaba0768 (2020).
- Kaiser, S. I. et al. Climate-controlled mass extinctions, facies, and sea-level changes around the Devonian–Carboniferous boundary in the eastern Anti-Atlas (SE Morocco). *Palaeogeogr. Palaeoclimatol. Palaeoecol.* 310, 340–364 (2011).
- Liu, J. S. et al. Intensified ocean deoxygenation during the end devonian mass extinction. *Geochem. Geophy. Geosy.* 20, 6187–6198 (2019).
- Zhang, F. et al. Extensive marine anoxia associated with the Late Devonian Hangenberg Crisis. Earth Planet. Sci. Lett. 533, 115976 (2020).
- Li, S. et al. Carbonate shutdown, phosphogenesis and the variable style of marine anoxia in the late Famennian (Late Devonian) in western Laurentia. *Palaeogeogr. Palaeoclimatol. Palaeoecol.* 589, 110835 (2022).
- Sahoo, S. K. et al. Basin-scale reconstruction of euxinia and Late Devonian mass extinctions. *Nature* 615, 640–645 (2023).
- Qie, W. K. et al. Enhanced continental weathering as a trigger for the end-devonian hangenberg crisis. *Geophy. Res. Lett.* 50, e2022GL102640 (2023).
- Caplan, M. L. & Bustin, R. M. Devonian–Carboniferous Hangenberg mass extinction event, widespread organic-rich mudrock and anoxia: causes and consequences. *Palaeogeogr. Palaeoclimatol. Palaeoecol.* 148, 187–207 (1999).
- Qie, W. K. et al. Local overprints on the global carbonate δ¹³C signal in Devonian–Carboniferous boundary successions of South China. *Palaeogeogr. Palaeoclimatol. Palaeoecol.* 418, 290–303 (2015).
- 13. Over, D. J. The Devonian-Carboniferous boundary in the United States. *Palaeobio. Palaeoenv.* **101**, 529–540 (2021).
- Pisarzowska, A. et al. Large environmental disturbances caused by magmatic activity during the Late Devonian Hangenberg Crisis. Glob. Planet. Change 190, (2020). 103155.
- Racki, G., Marynowski, L. & Rakocinski, M. Anomalous Upper Devonian mercury enrichments: comparison of Inductively Coupled Plasma-Mass Spectrometry (ICP-MS) and Atomic Absorption Spectrometry (AAS) analytical data. Geol. Quart. 62, 487–495 (2018).

- Kalvoda, J. et al. Mercury spikes at the Devonian-Carboniferous boundary in the eastern part of the Rhenohercynian Zone (central Europe) and in the South China Block. *Palaeogeogr. Palaeoclimatol. Palaeoecol.* 531, 109221 (2019).
- Paschall, O. et al. The Devonian-Carboniferous boundary in Vietnam: sustained ocean anoxia with a volcanic trigger for the Hangenberg Crisis?. Glob. Planet. Change 175, 64–81 (2019).
- Kaiho, K. et al. Coronene, mercury, and biomarker data support a link between extinction magnitude and volcanic intensity in the Late Devonian. *Glob. Planet. Change* 199, (2021). 103452.
- Marynowski, L. & Filipiak, P. Water column euxinia and wildfire evidence during deposition of the Upper Famennian Hangenberg event horizon from the Holy Cross Mountains (central Poland). *Geol. Mag.* 144, 569–595 (2007).
- Martinez, A. M. et al. A stable and productive marine microbial community was sustained through the end-Devonian Hangenberg Crisis within the Cleveland Shale of the Appalachian Basin, United States. *Geobiology* 17, 27–42 (2019).
- Marynowski, L. et al. Deciphering the upper Famennian Hangenberg Black Shale depositional environments based on multi-proxy record. *Palaeogeogr. Palaeoclimatol. Palaeoecol.* 346–347, 66–86 (2012).
- Hedhli, M. et al. Multiple diachronous "Black Seas" mimic global ocean anoxia during the latest Devonian. Geology. Geology 51, 973–977 (2023).
- Grasby, S. E. et al. Mercury as a proxy for volcanic emissions in the geologic record. *Earth-Sci. Rev.* 196, 102880 (2019).
- Percival, L. M. E. et al. Globally enhanced mercury deposition during the end-Pliensbachian extinction and Toarcian OAE: a link to the Karoo-Ferrar Large Igneous Province. *Earth Planet. Sci. Lett.* 428, 267–280 (2015).
- 25. Grasby, S. E. et al. Isotopic signatures of mercury contamination in latest Permian oceans. *Geology* **45**, 55–58 (2017).
- Them, T. R. et al. Terrestrial sources as the primary delivery mechanism of mercury to the oceans across the Toarcian Oceanic Anoxic Event (Early Jurassic). Earth Planet. Sci. Lett. 507, 62–72 (2019).
- Blum, J. D., Sherman, L. S. & Johnson, M. W. Mercury isotopes in Earth and environmental sciences. *Annu. Rev. Earth Planet. Sci. Lett.* 42, 249–269 (2014).
- Wang, X. D. et al. Mercury anomalies across the end Permian mass extinction in South China from shallow and deep water depositional environments. *Earth Planet. Sci. Lett.* 496, 159–167 (2018).
- Huang, Y. G. et al. Biotic responses to volatile volcanism and environmental stresses over the Guadalupian-Lopingian (Permian) transition. *Geology* 47, 175–178 (2019).
- Zheng, W. et al. Mercury isotope. signatures record photic zone euxinia in the Mesoproterozoic ocean. *Proc. Natl. Acad. Sci. USA*. 115, 10594–10599 (2018).
- Zheng, W. et al. Mercury isotope evidence for recurrent photic-zone euxinia triggered by enhanced terrestrial nutrient inputs during the Late Devonian mass extinction. *Earth Planet. Sci. Lett.* 613, 118175 (2023).
- Zheng, W. et al. Recurrent photic zone euxinia limited ocean oxygenation and animal evolution during the Ediacaran. *Nat. Commun.* 14, (2023). 3920.
- 33. Sun, R. Y. et al. Mercury isotope evidence for marine photic zone euxinia across the end-Permian mass extinction. *Commun. Earth Environ.* **4**, 159 (2023).
- Liu, M. et al. Mercury isotope evidence for Middle Ordovician photiczone euxinia: Implications for termination of the Great Ordovician biodiversification event. *Gondwana Res.* 137, 131–144 (2025).
- Wilkin, R. T., Barnes, H. L. & Brantley, S. L. The size distribution of framboidal pyrite in modern sediments. *Geochim. Cosmochim. Acta* 60, 3897–3912 (1996).

- Bond, D. P. G. & Wignall, P. B. Pyrite framboid study of marine Permian–Triassic boundary sections: a complex anoxic event and its relationship to contemporaneous mass extinction. *Geol. Soc. Amer. Bull.* 122, 1265–1279 (2010).
- German, C. R., Holliday, B. P. & Elderfield, H. Redox cycling of rare earth elements in the suboxic zone of the Black Sea. *Geochim.* Cosmochim. Acta 55, 3553–3558 (1991).
- Tostevin, R. et al. Low-oxygen waters limited habitable space for early animals. Nat. Commun. 7, 1–9 (2016).
- Nesbitt, H. W. & Young, G. M. Early Proterozoic climates and plate motions inferred from major element chemistry of lutites. *Nature* 299, 715–717 (1982).
- Fendley, I. M. et al. Early Jurassic large igneous province carbon emissions constrained by sedimentary mercury. *Nat. Geosci.* 17, 241–248 (2024).
- Sherman, L. S. et al. Mercury isotopic composition of hydrothermal systems in the Yellowstone Plateau volcanic field and Guaymas Basin seafloor rift. *Earth Planet. Sci. Lett.* 279, 86–96 (2009).
- Zambardi, T. et al. Mercury emissions and stable isotopic compositions at Vulcano Island (Italy). Earth Planet. Sci. Lett. 277, 236–243 (2009).
- 43. Si, M. et al. Measurement of atmospheric mercury over volcanic and fumarolic regions on the North Island of New Zealand using passive air samplers. *ACS Earth Space. Chem.* **4**, 2435–2443 (2020).
- 44. Bergquist, B. A. & Blum, J. D. Mass-dependent and -independent fractionation of Hg isotopes by photoreduction in aquatic systems. *Science* **318**, 417–420 (2007).
- Yin, R. et al. Identifying the sources and processes of mercury in subtropical estuarine and ocean sediments using Hg isotopic composition. *Environ. Sci. Technol.* 49, 1347–1355 (2016).
- Thibodeau, A. M., et al. Mercury anomalies and the timing of biotic recovery following the end-Triassic mass extinction. *Nat. Commun.* 7, 11147 (2016).
- Zhao, H., et al. Mercury isotope evidence for regional volcanism during the Frasnian-Famennian transition. *Earth Planet. Sci. Lett.* 581, 117412 (2022).
- Zhao, H. et al. Mercury enrichments during the Carnian Pluvial Event (Late Triassic) in South China. Geol. Soc. Amer. Bull. 134, 2709–2720 (2022).
- Song, Y. et al. Biomarker evidence of algal-microbial community changes linked to redox and salinity variation, Upper Devonian Chattanooga Shale (Tennessee, USA). *Geol. Soc. Am. Bull.* 133, 409–424 (2021).
- Sun, R. Y. et al. Modelling the mercury stable isotope distribution of Earth surface reservoirs: implications for global Hg cycling. *Geochim. Cosmochim. Acta* 246, 156–173 (2019).
- Zheng, W. & Hintelmann, H. Isotope fractionation of mercury during its photo-chemical reduction by low-molecular-weight organic compounds. J. Phys. Chem. A 114, 4246–4253 (2010).
- 52. Motta, L. C. et al. Mercury isotope fractionation during the photochemical reduction of Hg (II) coordinated with organic ligands. *J. Phys. Chem. A* **124**, 2842–2853 (2020).
- Zheng, W. et al. Mercury stable isotope fractionation during abiotic dark oxidation in the presence of thiols and natural organic matter. *Environ. Sci. Technol.* 53, 1853–1862 (2019).
- 54. Bond, D. P. G. & Grasby, S. E. On the causes of mass extinctions. *Palaeogeogr. Palaeoclimatol. Palaeoecol.* **478**, 3–29 (2017).
- Yao, L. et al. The longest delay: re-emergence of coral reef ecosystems after the Late Devonian extinctions. *Earth-Sci. Rev.* 203, 103060 (2020).
- Joachimski, M. M. et al. Devonian climate and reef evolution: insights from oxygen isotopes in apatite. *Earth Planet. Sci. Lett.* 284, 599–609 (2009).
- 57. Cramer, B., Saltzman, M., Day, J. E. & Witzke, B. J. Record of the Late Devonian Hangenberg global positive carbon-isotope excursion in an

- epeiric sea setting: carbonate production, organic-carbon burial and paleoceanography during the Late Famennian. *Geol. Assoc. Canada Spec. Pub.* **48**, 103–118 (2008).
- Kaiser, S. I., Steuber, T. & Becker, R. T. Environmental change during the Late Famennian and Early Tournaisian (Late Devonian–Early Carboniferous): implications from stable isotopes and conodont biofacies in southern Europe. *Geol. J.* 43, 241–260 (2008).
- Prestianni, C. et al. The terrestrialization process: modelling complex interactions at the biosphere-geosphere interface. *Geol. Soc. London Spec. Pub.* 339, 71–80 (2010).
- D'Antonio, M. P., Ibarra, D. E. & Boyce, C. K. Land plant evolution decreased, rather than increased, weathering rates. *Geology* 48, 29–33 (2020).
- 61. Hedhli, M. et al. Devonian to Carboniferous continental-scale carbonate turnover in Western Laurentia (North America): upwelling or climate cooling?. *Facies* **68**, (2022). 15.
- Qie, W. K. et al. Devonian-Carboniferous boundary in China. Palaeobio. Palaeoenv. 101, 589–611 (2021).
- 63. Johnston, D. I., Henderson, C. M. & Schmidt, M. J. Upper Devonian to Lower Mississippian conodont biostratigraphy of uppermost Wabamun Group and Palliser Formation to lowermost Banff and Lodgepole formations, southern Alberta and southeastern British Columbia, Canada: implications for correlations and sequence stratigraphy. Bull. Can. Petrol. Geol. 58, 295–341 (2010).
- 64. Liu, Y. S. et al. Geochemistry and magmatic history of eclogites and ultramafic rocks from the Chinese continental scientific drill hole: subduction and ultrahigh–pressure metamorphism of lower crustal cumulates. *Chem. Geol.* 247, 133–153 (2008).
- Huang, Q. et al. An improved dual–stage protocol to pre–concentration mercury from airborne particles for precise isotopic measurement. J. Anal. At. Spectrom. 30, 957–966 (2015).
- 66. Bergquist, B. A. & Blum, J. D. Mass-dependent and independent fractionation of Hg isotopes by photoreduction in aquatic systems. *Science* **318**, 417–420 (2007).
- Wang, X. D. et al. Mercury anomalies across the Cryogenian-Ediacaran boundary in South China. *Precambrian Res.* 379, 106771 (2022).
- 68. Wang, X. D. et al. Global mercury cycle during the end-Permian mass extinction and subsequent Early Triassic recovery. *Earth Planet. Sci. Lett.* **513**, 144–155 (2022).
- Sun, G. Y. et al. Mass-dependent and independent fraction of mercury vapor by atomic Cl and Br. *Environ. Sci. Technol.* 50, 9232–9241 (2016).

Acknowledgements

We are grateful to Chao Zhang and Ke Zhang for their help with Hg isotope analyses, to Swapan Sahoo and two anonymous reviewers for their helpful comments that improved this manuscript, to Dr. Carolina Ortiz Guerrero and Dr. Holly Stein for their exceptional dedication and meticulous efforts in handing the manuscript. This study was supported by National Natural Science Foundation of China (42488101, 42472160, 42477215, 92055212, and 42003057), Australian Research Council grant (FL160100168), the "CUG Scholar" Scientific Research Funds at China University of Geosciences (Wuhan) (Project No.: 2023081), the China Postdoctoral Science Foundation (GZC20232474, 2024M753028), the Postdoctoral Project of Hubei Province (2004HBBHCXA084), and Special Fund from State Key Laboratory of Geological Processes and Mineral Resources, China University of Geosciences (MSFGPMR2024-104). No sampling permissions were required in this study.

Author contributions

X.W., H.Z., F.H., G.S., and P.C designed the project; X.W., H.Z., S.G., M.H., and Z.L. conducted field work, stratigraphic analyses, and sampling; X.W., H.Z., S.G., and M.H. conducted carbon isotopic and elemental analyses; X.W., H.Z., and G.S. carried out Hg isotopic analyses; X.W. and Z.-Q.C.

conducted pyrite framboid morphology analyses; X.W. wrote the paper with inputs from H.Z., S.G., P.C., M.H., Z.-Q.C., and F.H. All authors contributed to the final version.

Competing interests

The authors declare no competing interests.

Additional information

Supplementary information The online version contains supplementary material available at https://doi.org/10.1038/s43247-025-02260-x.

Correspondence and requests for materials should be addressed to He Zhao or Guangyi Sun.

Peer review information Communications Earth & Environment thanks Swapan K Sahoo and the other, anonymous, reviewer(s) for their contribution to the peer review of this work. Primary Handling Editors: Holly Stein and Carolina Ortiz Guerrero. A peer review file is available.

Reprints and permissions information is available at http://www.nature.com/reprints

Publisher's note Springer Nature remains neutral with regard to jurisdictional claims in published maps and institutional affiliations.

Open Access This article is licensed under a Creative Commons Attribution-NonCommercial-NoDerivatives 4.0 International License, which permits any non-commercial use, sharing, distribution and reproduction in any medium or format, as long as you give appropriate credit to the original author(s) and the source, provide a link to the Creative Commons licence, and indicate if you modified the licensed material. You do not have permission under this licence to share adapted material derived from this article or parts of it. The images or other third party material in this article are included in the article's Creative Commons licence, unless indicated otherwise in a credit line to the material. If material is not included in the article's Creative Commons licence and your intended use is not permitted by statutory regulation or exceeds the permitted use, you will need to obtain permission directly from the copyright holder. To view a copy of this licence, visit http://creativecommons.org/licenses/bync-nd/4.0/.

© The Author(s) 2025